




SAR SENTINEL-1 DATA, NDFI AND NDFVI FOR DETECTING AND MAPPING THE FLOOD HAZARD IN OUED SAKIA-EL HAMRA (LAAYOUNE, SOUTH MOROCCO)

Mohammed MOURJANE ^{1*}, Naoual EL HAMMOUCH ¹, Hassan TABYAOUI ¹, Fatima EL HAMMACHI ¹, Fatima-Zahra LAAREJ ¹, Nassareddine AZZOUZI ¹, Ahmed GABER ²

DOI: 10.21163/GT_2024.192.19

ABSTRACT

A new automated approach for flash extent delineation and mapping and risk assessment was applied in the context of the Oued Sakia-Al Hamra flood (Laayoune, southern Morocco) of October 2016. Normalized Difference Flood Index (NDFI) mapping was employed to distinguish between flood-prone and non-flood-prone areas across an extensive region, leveraging the Bragg backscattering properties of active radar pulses on flat water surfaces, which exhibit minimal signal reflection. The study utilized Sentinel-1 satellite SAR images in Wide Swath (IW) interferometric mode and Ground Range Detected (GRD) product type. Pre-processing and processing chain, which combines water classification, multi-temporal and contextual filtering, topographic correction of a total number of 2 images: before and after the flood event. Consequently, a high classification accuracy of 99.05% using Sentinel-1 C-band images for the flooded area of Oued Sakia-El Hamra was obtained after validation using both optical images of Landsat-8 and Google-Earth. The results demonstrate the effective utilization of SAR data for identifying flooded areas, assessing their extent, evaluating associated hazards, and subsequently recommending appropriate mitigation measures as needed.

Key-words: SAR data, scattering response, natural flooding, Sakia-Al Hamra River, Morocco.

1. INTRODUCTION

Flash floods occur in numerous regions worldwide, causing substantial annual losses (White, 2023). They represent the most common natural disaster and are recognized as a significant threat, particularly in urban areas across sub-Saharan Africa (Tiepolo, 2014). Since, accurately mapping the flooded water extent areas is very important to be used to validate the hydraulic models and quantify the flood risk consequences in the context of land use planning and coverage.

Floods frequently inundate expansive regions that are challenging to survey and monitor on the ground. Spatial remote sensing data serves as an ideal source for efficiently and cost-effectively monitoring large-scale flood events from a bird's-eye view. Optical satellite imagery, including platforms like QuickBird, RapidEye, Planet, Landsat, SPOT, ASTER, Sentinel-2, and MODIS, has proven effective in previous studies for generating water masks of flooded areas. These optical sensors represent the most favored source of information due to their spectral component and simplicity of interpretation (Smith, 1995). Usually, such optical satellite data are suffered from cloud covers, especially of those which are accompany the heavy rains and cause flooding (Henshaw et al., 2013; Schumann et al., 2018). Meanwhile, synthetic aperture radar (SAR) systems emerge as robust tools for flood monitoring in near-real-time (NRT), owing to their ability to operate effectively in diverse

¹Natural resources and Environment Laboratory, Polydisciplinary Faculty of Taza, Sidi Mohamed Ben Abdellah University, Fez, Morocco, corresponding author* mourjanemohammed@gmail.com, naouallelhammouch@gmail.com, hassan.tabyaoui@usmba.ac.ma, fatima.elhammichi@usmba.ac.ma, laarej.fatimazahra96@gmail.com, Nassareddine.azzouzi@usmba.ac.ma.

² Faculty of Science, Port Said University, Egypt, ahmedgaber_881@hotmail.com

weather conditions (Mertes, 2002; Alsdorf et al., 2007) and around the clock (Franceschetti & Lanari, 1999; Schumann & Moller, 2015). SAR technology has demonstrated proficiency in detecting water surfaces, estimating flood depths, and identifying submerged areas under canopy cover. Significant efforts have been devoted to development of algorithms for accurately delineating flood extents from radar imagery. Common methodologies for SAR-based flood mapping encompass simple visual interpretation, supervised classification, image texture analysis, threshold segmentation, histogram-based thresholding, multi-temporal change detection techniques, active contour models, and interferometric SAR approaches (Arnesen et al., 2012 ; Borghys et al., 2006 ; Brivio et al., 2002 ; Dellepiane & Angiati, 2012 ; Dellepiane et al., 2000 ; Di Baldassarre et al., 2011 ; Dong et al., 2015 ; Horritt et al., 1999 ; 2001 ; Hostache et al., 2012 ; Martinez & Le Toan, 2007 ; Martinis et al. 2011 ; Mason et al., 2007 ; Nico et al., 2000 ; Pierdicca et al., 2012 ; Pulvirenti et al., 2011 ; 2013 ; Schumann et al., 2009 ; Smith, 1997).

Change Detection (CD) method involves technology that compares backscatter intensity before and during flooding to identify pixel change (Mertes, 2002; Alsdorf et al., 2007; Lu et al., 2014). The main water body thus identified from the reference image is used on the flood image to isolate water pixels within these bodies, facilitating the derivation of statistical curves that describe them.

By combining the strengths of change detection (CD) and thresholding, Long et al. (2014) computed the absolute difference between flood and reference images and applied two thresholds to distinguish flood areas and shallow water within short vegetation. To enhance objectivity and reduce user influence, threshold values were derived by analyzing the histogram of the difference image through a mathematical formula. In a similar vein, Cian et al. (2018) have devised two flood indices based on the methodology introduced by Long et al. (2014). The Normalized Difference Flood Index (NDFI) and the Normalized Difference Flood in Short Vegetation Index (NDFVI) function primarily as change detection techniques (Cian et al., 2018). They offer advantages such as reduced reliance on manual intervention and swift flood mapping capabilities (Xue et al., 2022). Specifically, NDFI categorizes flooded regions based on the disparity between the mean and minimum backscatter coefficient values across a time series (Álvarez-Mozos et al., 2005). However, NDFVI is tailored to highlight shallow water within areas of short vegetation, assuming sufficient revisit times for each pixel under dry conditions. This differentiation is crucial given the influence of factors like wind, vegetation, and environmental variability arising from satellite system parameters. The overarching goal of this study is to document and assess temporal and spatial changes in surface conditions of streams before and after flooding in the desert environment of the Moroccan Sahara. Like Cian et al. (2018), the approach prioritizes robustness and simplicity, requiring minimal user input and demonstrating effective applicability across diverse environments using data from various sensors. Additionally, it excels in delineating shallow water within short vegetation and identifying flooded open areas.

2. ENVIRONMENTAL SETTING OF THE STUDY SITE

The study area lies in the interior of the Moroccan Sahara (**Fig. 1A**), in particular the Oued Sakia El Hamra, which flows through one of the largest cities in the Moroccan Sahara (Laayoune Town). The area stretches from the foot of the Anti-Atlas massif to the town of Lagouira in the south and the Atlantic coast in the west (**Fig. 1B**). It is physically remarkably homogeneous, with a large desert zone characterized by the presence of the hammada, essentially made up of immense desert plateaus. The relief is very flat. Its monotony is interrupted only by a few sabkhas (depressions), limited dune belts and the remnants of a fairly small hydrographic network. The geological bedrock consists of Upper Cretaceous limestones and sandstones, dipping very gently to the west and overlain by powerful Oligocene and Miocene unconformable beds (Ratschiller, 1970). The top of the series is composed of lithological formations of Tertiary to Quaternary age, consisting of dunes, sands, evaporated silts and carbonate sandstones.

The area is crossed by the Sakia Hamra wadi, which is the source of numerous dry tributaries, highly parched valleys. In normal periods, the flow of the wadi is considered negligible, due to the

obstruction of its lower valley by a corridor of sand dunes moving from south to north, associated with landslides, the presence of the "Al Massira Al Khadra" hill dam built in 1995 at the town of Laayoune, and the absence of floods that have reached the ocean for over fifty years. Further west, this watercourse is now marked on the edge of the town of Laayoune by linear tree vegetation supported by the water table in the shallow subsoil.

The study area experiences moderate temperatures influenced by its proximity to the Atlantic Ocean. Annual rainfall is minimal, averaging 59 mm at the Laayoune station, and occurs irregularly. Coastal temperatures range from 17 to 25°C throughout the year. Persistent winds prevail across the region, with monthly maximum speeds ranging from 15.4 to 19.2 m/s, and an annual average speed of approximately 17.6 m/s or 63.4 km/h (HCP, 2020). Due to its consistency and strength, wind plays a crucial role in generating silting phenomena, shaping dune landscapes, and influencing sand movement dynamics. The dunes near Laayoune are renowned for being among the fastest-moving in the world, averaging a migration rate of 32 meters per year for dunes that are 9 m high tall. The dune fields take the form of a river of sand running NNE-SSW over a length of 150 km. Geomorphologically, the barchan dune is the dominant dune form in the region (Amimi et al., 2017). Air circulation patterns are significantly shaped by the coastline's configuration, while the dune formations are intricately connected to loose sediments originating from the Sahara (Fig. 1C).

In October 2016, this region was hit by violent storms that caused impressive flooding and river flooding. The rainfall occurred over a ten-hour period (between October 28 and 29). The volume of water stored at the Al Massira Al Khadra dam, which is known to have a total storage capacity of 110 million m³. The flood's peak was reached over 3,000 m³/s, well above the spillway's storage capacity threshold (410 m³/s). The occurrence of this extraordinary flood resulted in the wadi overflowing the crest of the dam, causing damage to the downstream slope. The height of the two breaches then increased as the overflow gradually reached the level of the river. The flood of October 28-30, 2016 swept away the entire infrastructure in the lower valley and led to the failure of the dam by overflow, followed by the obliteration of the dunes in the lower valley and delta (Mazel et al., 2019).

The infrastructure of the city of Laayoune concerns a wide range of sectors, from transport to energy, water, education, health, urbanization, agriculture, fisheries and food (HCP, 2020). They have undergone further development with projects to set up a technopole in the dried-up mouth of the Sakia El Hamra wadi (Mazel et al., 2019). This phenomenon, combined with the higher intensity of floods, has led to an increase in losses and damages.

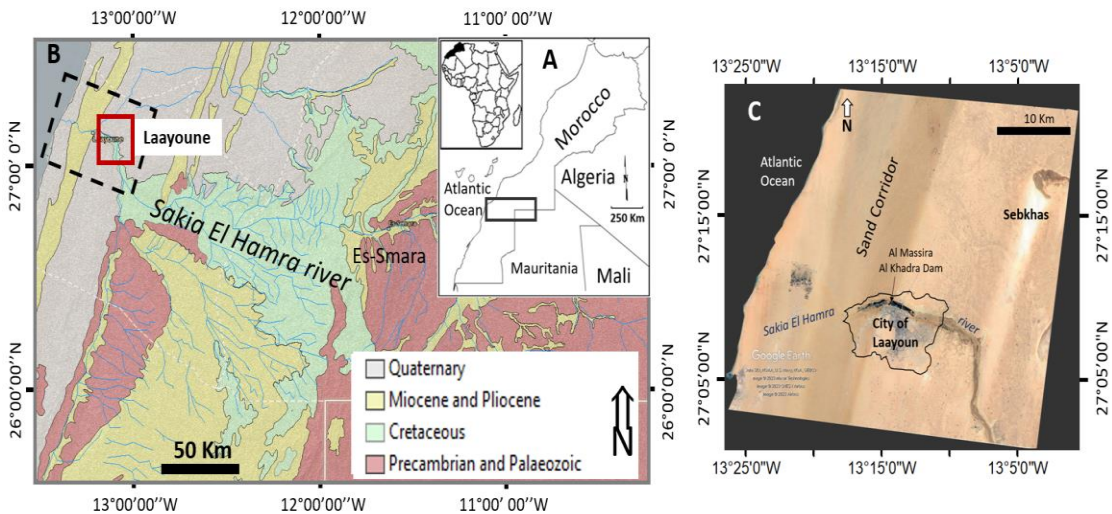


Fig. 1. A - Position of studied area in the south of Morocco, B - Simplified geological map of the study area from Geological map of Morocco at 1/1000000, and C - Situation of the study area in Google Earth image.

3. MATERIALS AND METHODS

Sentinel-1 mission represents a pivotal advancement, harnessing Earth Observation (EO) megadata with its provision of free, global SAR measurements through numerous repetitive observations. In this study, Sentinel-1 Level-1 Ground Range Detected (GRD) products were utilized. These products consist of focused, multi-look SAR data that have been geocoded onto the Earth's surface using a terrestrial ellipsoid model such as WGS84. The Sentinel-1 images employed in this study belong to the wide interferometric SAR category and operate within the C-band frequency range. They were accessed from the Sentinels Scientific Data Hub (<https://scihub.esa.int/>). The acquired images underwent processing using the Sentinel Application Platform (SNAP) software, which is an open-source framework developed by the European Space Agency (ESA) designed for the comprehensive exploitation and analysis of Earth Observation (EO) data (<http://step.esa.int>).

The methodology involves creating two sets of image stacks (**Fig. 2**) one comprising reference images and another incorporating flood images under investigation. Both stacks undergo radiometric calibration and terrain correction. Temporal statistics are computed thereafter to calculate the Normalized Difference Flood Index (NDFI) for detecting temporary open water bodies. The Normalized Difference Flood Index in Vegetated Areas (NDFVI) was computed to detect shallow water within short vegetation. Subsequently, a threshold is applied to the index values to isolate flooded areas, followed by additional filtering to eliminate clusters of erroneous pixels and enhance the precision of the final flood mapping results.

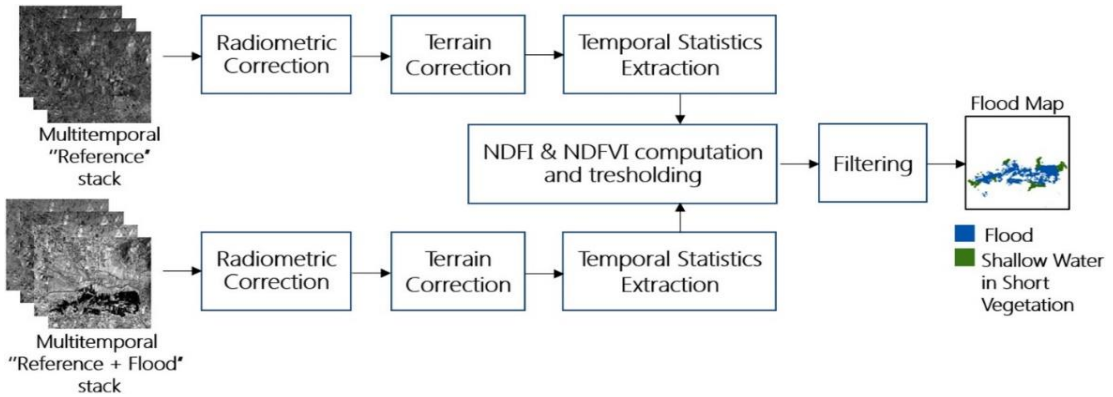


Fig. 2. Overview of method adopted in this study (after Cian et al., 2018).

The NDFI and NDFVI calculation formulas are as follows:

$$\text{NDFI} = \frac{\text{mean}(\sigma_0 \text{ reference}) - \min(\sigma_0 \text{ reference}, \sigma_0 \text{ flood})}{\text{mean}(\sigma_0 \text{ reference}) + \min(\sigma_0 \text{ reference}, \sigma_0 \text{ flood})} \quad (1)$$

$$\text{NDFVI} = \frac{\text{mean}(\sigma_0 \text{ reference}) - \max(\sigma_0 \text{ reference}, \sigma_0 \text{ flood})}{\text{mean}(\sigma_0 \text{ reference}) + \max(\sigma_0 \text{ reference}, \sigma_0 \text{ flood})} \quad (2)$$

among these terms, "mean" ("reference") signifies the average backscatter coefficient of each pixel in the reference image, while "min" ("reference + flood") denotes the minimum backscatter coefficient of each pixel across all images.

We mention that in normal cases, Manjusree et al., (2012) show that backscatter of flood water in HV and VH polarizations are same, and both HV and VH polarizations are adequate for flood water mapping. From near range to far range, -8 to -12 dB, -15 to -24 dB and -6 to -15 dB can be used as optimal ranges for flood water classification in HH, HV and VV polarizations. This study can be the blueprint to define optimal threshold ranges of NDFI and NDFVI to produce flood maps within a short time from the onset of disasters and deliver these maps to the concerned agencies.

4. SURFACE ROUGHNESS ANALYSIS

The C-band, operating at a central frequency of 5.405 GHz and a wavelength of 5.7 cm, exhibits high sensitivity to surface water content as observed by radar. This characteristic means that this band can be utilized across various applications, such as soil moisture measurement and flood detection. In the filtered and geocoded reference image (**Fig. 3A**), the smoother surfaces appear very dark (Bragg scattering), attesting to the fact that the depth of penetration of radar waves into this bare dry soil can be quite deep. Radar waves can thus map bedrock and gravel surfaces beneath wind-blown sand several centimeters, or even meters, thick. This confirms that the highest soil layers detected can be considered as a homogeneous dielectric medium. Rough surfaces, which appear very bright on a radar image, correspond to SSW-NNE corridor of moving sand dunes. These have different geometric and dielectric properties, with backscattering on rough surfaces. With the same textural properties on the ground, image B (**Fig. 3B**) taken after the rainy flood period shows strong backscattering of the radar signal. This confirms that the dielectric properties of soil depend on its water content, and that the backscatter coefficient measured by radar instruments increases with increasing in soil moisture.

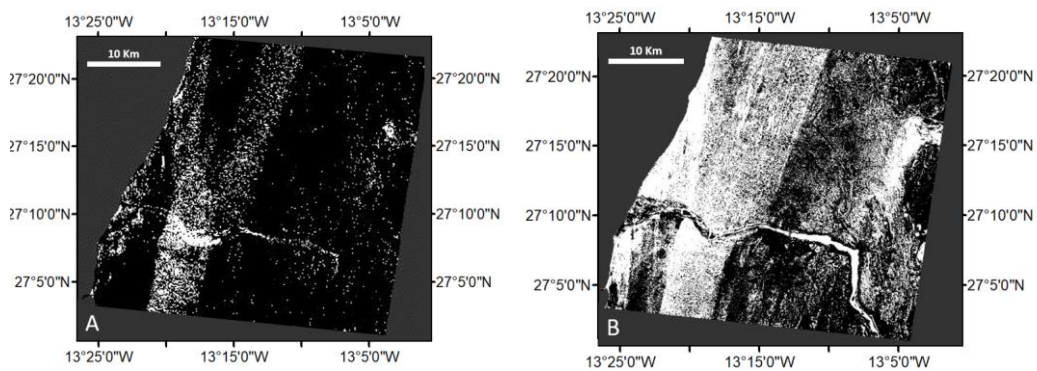


Fig. 3. Filtered and geocoded reference (A) and after flood event (B) of the study area.

Radar backscatter refers to the amount of radar signal redirected back to the sensor by the target (ESA, 2022). The backscatter coefficient, denoted as σ_0 (Sigma0), is typically measured in decibels (dB) (Rosenqvist et al., 2018). In SAR imagery interpretation, a general principle states that rougher surfaces exhibit higher backscatter intensity in both cross-polarized and co-polarized orientations, resulting in brighter images (Liew 2001). Conversely, smooth surfaces tend to produce specular reflections, where radar signals are directed away from the sensor, leading to reduced radar return. Rough surfaces, on the other hand, scatter radar signals in various directions, resulting in greater radar return (IPR, 2022).

In semi-arid and arid landscapes, land surfaces are generally having low soil moisture content and making the radar backscattered return is mainly from the soil roughness, vegetation cover and rocks. Surface roughness is a dynamic geomorphic property. Radar signals vary considerably. In the study area, the radar signal returned varies significantly due to changes in terrain morphology, topography, and the predominance of sandy surface cover (**Fig. 4**).

On the reference corrected image centered on the course of Oued Sakia El Hamra (**Fig. 4A**), and for pixels with values σ_0 less than 0.007dB (Points 1 to 6), water bodies are delineated with high precision, focusing on accurately detecting their outer boundaries. This is the case for pixels located in the middle of the dam (Points 1 and 2). These values are also detected in the target image (**Fig. 4B**). For σ_0 values between 0.009 and 0.012, backscattering from the sand dunes on the bed of the main watercourse is expected (Points 9 to 12). For σ_0 values between 0.012 and 0.0135, the water mass limits are included (Points 13 to 17). Values of σ_0 between 0.062 to 0.067 (Points 20 to 23) attest to a smooth surface and the image are dark. By increasing this threshold ($\sigma_0 > 0.138$) (Points 7,

8, 18 and 19), dry pixels of bare soil in watercourses begin to be included. Once the watercourse is fed, these pixels give values of σ_0 around 0.0034 (Point 7, **Fig. 4B**).

Sabkhas are mainly found in inland desert basins and nearby coasts with semi-arid and arid climates. These depressions mark the desert landscape of southern Morocco. Most of them cover less than 5 square kilometers. They are seasonally covered by water that gradually seeps into the underlying aquifers or evaporates, causing salt and sediment deposits to form at the bottom and edges, and shaping their surface properties. Deposited sediments are exposed to shrinkage and drying, and the clay layers contained control changes in sediment volume, as clay-rich layers cause deep sediment shrinkage and drying during long-term droughts.

Changes in their surface area are controlled by changes in groundwater supply and evapotranspiration. These regions show low backscatter on the radar signal from the dry period and, on the contrary, very high backscatters of the radar signal on the image taken during the wet period (Point 25, **Fig. 4A & 4B**). This suggests that the sensitivity of the radar backscatter coefficient to salinity is influenced by moisture content. The strong dependence of the backscatter coefficient on salinity for low humidity values is an important result for applications involving the detection of low water resurgence, and confirms the work of Lasne et al, (2009).

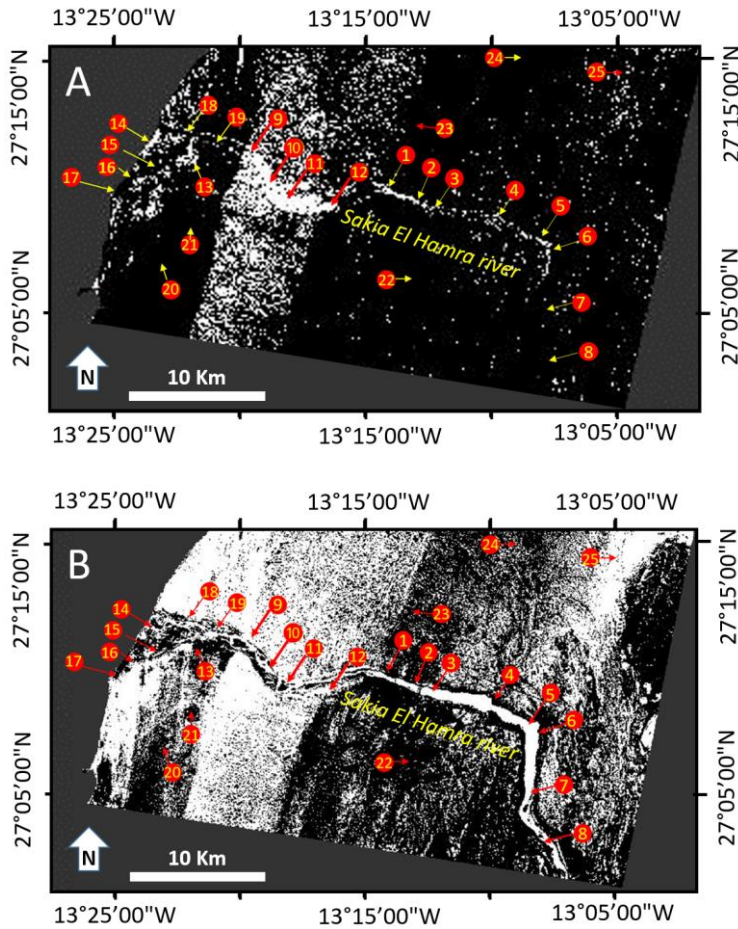


Fig. 4. Position of points with σ_0 values in the filtered and geocoded reference image (A) and after flood event (B) of the study area.

5. INDEX ANALYSIS

Fig. 5 displays the outcomes of the index analysis on the Google Earth image (A) the corresponding NDFI image and (B) the resulting NDFVI image. The blue color of the NDFI image is the water bodies that flood the city of Laayoune (σ_0 is around -0.93), in addition to the rivers that find their main beds under the moving sand dunes (σ_0) (**Fig. 5A**). The same map reports water bodies on bare soil. Pixels take on σ_0 values between -0.33 and 0.55. These pixels can be removed from the final maps, which is generally appropriate except in proximity to flooded areas where they may need to be included in the final flood map. The dilation filter helps mitigate this potential error, which remains within acceptable limits. On sand dunes, water bodies are barely distinguishable and σ_0 is around -0.20. This supports the idea that dunes fossilize impermeable layers and recharge water to deep aquifers.

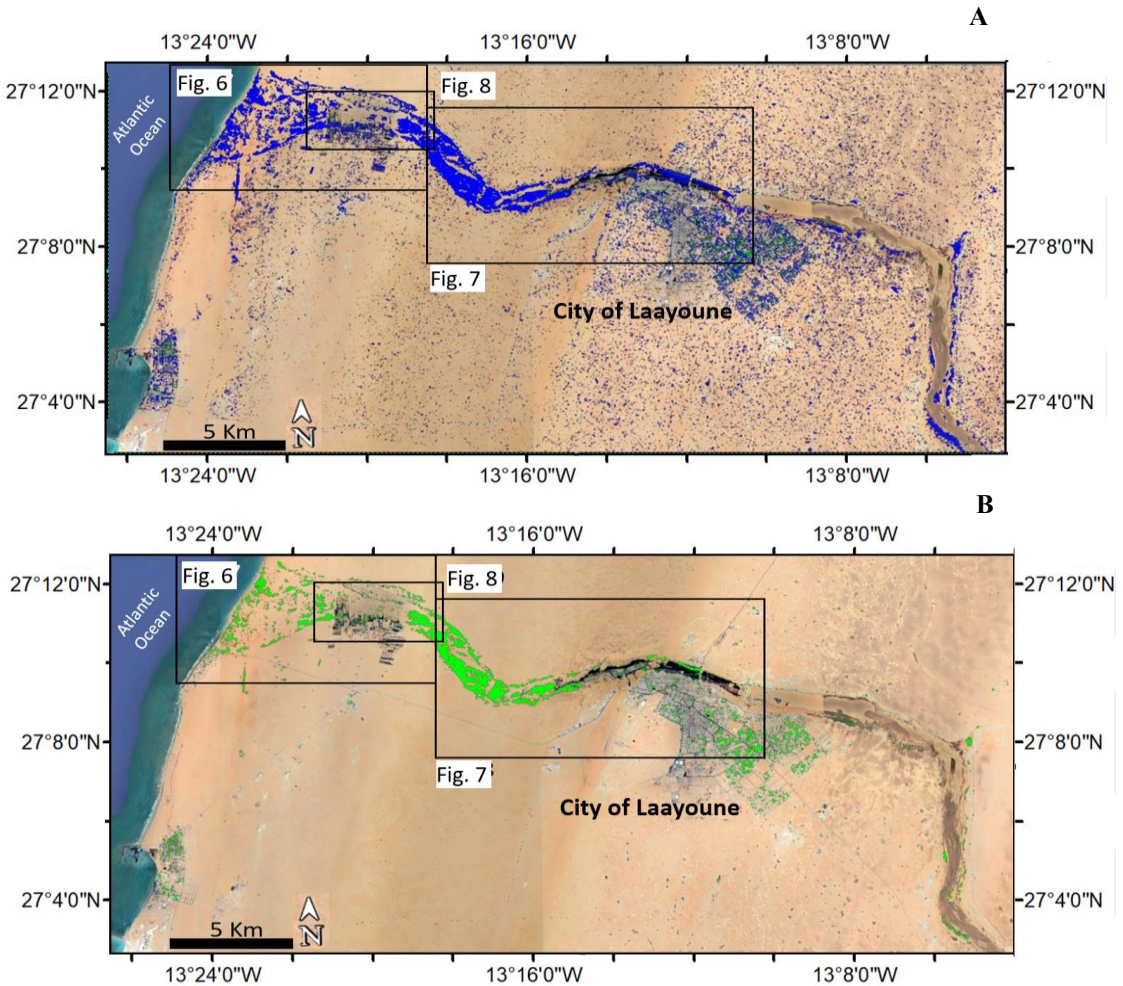


Fig. 5. Successively resulting analysis of NDFI and NDFVI on Google-Earth image of the study area (frames show positions of **Fig. 6, 7 and 8**).

The findings exhibit strong agreement with flooded areas identified by Hakdaoui et al., (2019) through their analysis of multi-spectral data in the same region. These researchers utilized four spectral indices (Normalized Difference Water Index "NDWI", Normalized Difference Moisture Index "NDMI", Normalized Difference Drought Index "NMDI", and Albedo "Al"), followed by

change detection using diachronic images data from Sentinel-2 MSI and Landsat-8 OLI acquisitions before and after the event. Their study underscores the value of integrating diverse sensor data for dynamic flood mapping purposes.

Fig. 5B illustrates the outcome of the NDFVI index analysis. Pixels aggregate prominently around the city, along the primary watercourse to the east, and at the river mouth, constituting more than 95% of all pixels classified as shallow water in short vegetation. In other areas, these pixels are scarcely discernible on the image.

6. RESULTS

Fig. 6 zooms in on a small area of the watercourse west of the town of Laayoune, where shallow water and short vegetation were detected by the NDFI and NDFVI indices. This is a time series of images from Google Earth referenced from the winter period from December 2010 to April 2023. The presence of bodies of stagnant water can be observed in numerous closed, endorheic depressions, generally limited by reliefs shaped by sand dunes. The latter occupy the route of the watercourse which is usually dry until the flood period. Depressions come from the dislocation of an organized hydrographic network, by capture, by exhaustion of flow or by drying out of the climate. They therefore depend on the climate and its variations over time. This zone gives an idea of the rate of accumulation of sand in depressions and lowlands. The rainy events that occurred in December 2016 were unusual and returned the main watercourse to its original path. This perfectly illustrates the interaction between aeolian and fluvial processes through the accumulation of sand resulting from an aeolian and fluvial process during dry conditions alternating with humid climatic episodes and the return of the fluvial system. Wind activities have led to the formation of a variety of dunes and sand sheets which promote the concentration of groundwater in humid periods. This is due to favorable circumstances often occurring in a desert environment.

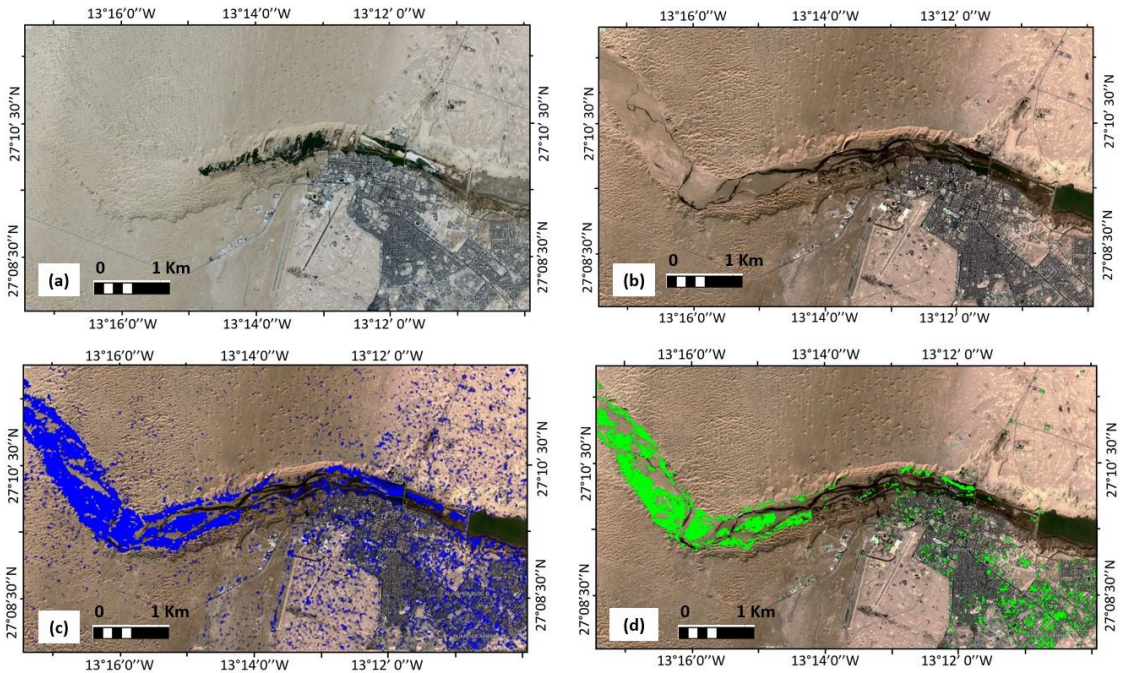


Fig. 6. Successively before (a) and after flood (b), NDFI (c) and NDFVI (d) along Sakia Al Hamra river and near Laayoune city.

The climate intervenes primarily in the specific profile of these bodies of water, which are all particular hydrological units. It regulates the abundance of rain, the primary source of water supply, and the evaporation, which counterbalances it. It also intervenes on the alternation regime between wet and dry periods. In addition to the direct contribution of rain, there are tributary contributions, diffuse runoff on the slopes and flooding in the rivers, when there is any, exsurgence and resurgence of groundwater.

Interpretation of spatial images at different scales provided the necessary indicators of the relationship between sand accumulations and fluvial processes. Sand accumulations would have been responsible for the concentration of groundwater in the substrate. Thus, the correlation between the likelihood of groundwater presence in depressions and substantial accumulations of sand emerges as a crucial consideration in the exploration of this progressively scarce resource.

Further west, near the mouth of Oued Sakia El Hamra, numerous drainage lines adjacent to the Foug El Oued aquifer were identified using NDFI and NDFI images. These dry waterways were covered in wind-blown sand. They generally reappear in sheet flood conditions with abundant surface water. Several of these large channels have small, braided streams in their layers, as revealed by enlargements of the Sentinel-1 data (**Fig. 7**). Braiding typically develops from small amounts of surface water, indicating multiple episodes of water flow. During the flood, the interior depositional basins would have accumulated significant volumes of fresh water. A large part of this water has been infiltrated in the deeper rocks under the sand. Field observations reveal that moisture starts to appear a few centimeters deep within the sand cover of shallow channels. Thus, areas that encompass large accumulations of sand may rely on vast groundwater resources.

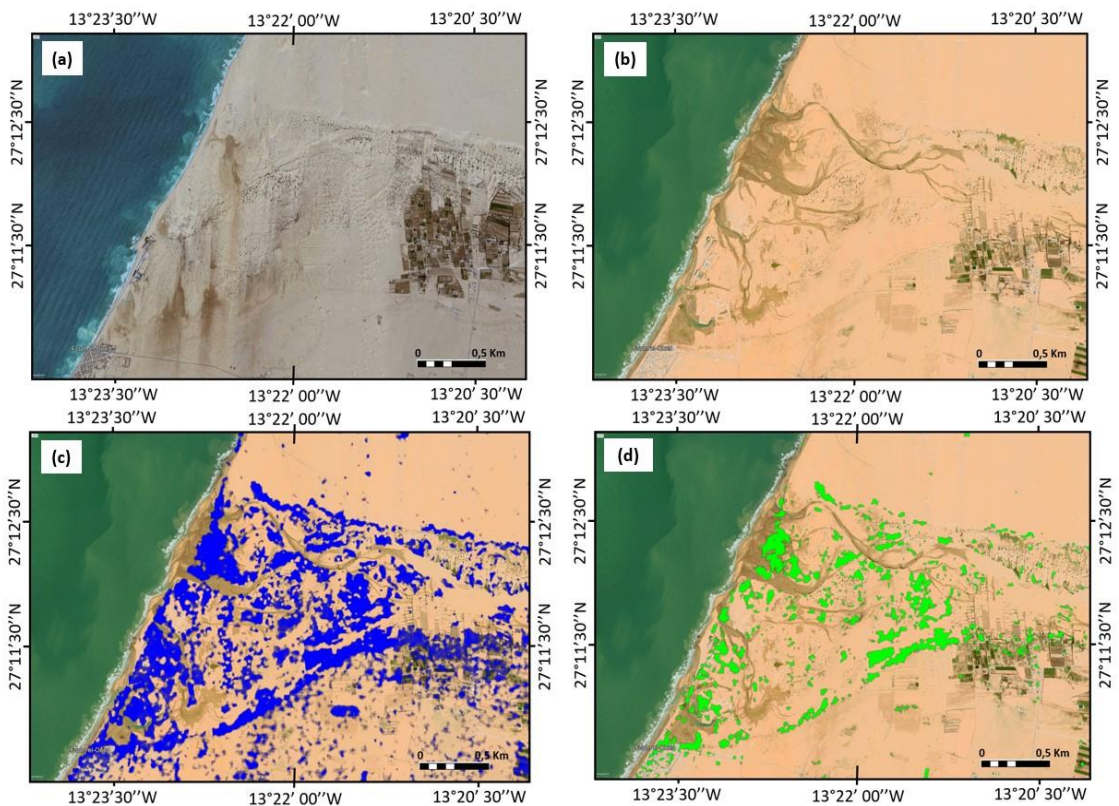


Fig. 7. Successively before (a) and after flood (b), NDFI (c) and NDFVI (d) at the mouth of Oued Sakia El Hamra in contact with the Atlantic Ocean.

In the collective imagination, the desert is synonymous with aridity. Researchers estimate the probability of urban flooding that could cause damage and threaten lives is less than 10% and the risk of flooding is considered very low or non-existent. To this end, many constructions are installed in areas prone to flooding. Due to its relatively flat topography, gentle slopes, and clay-rich layers, the torrential rains resulted in significant economic losses and material damage.

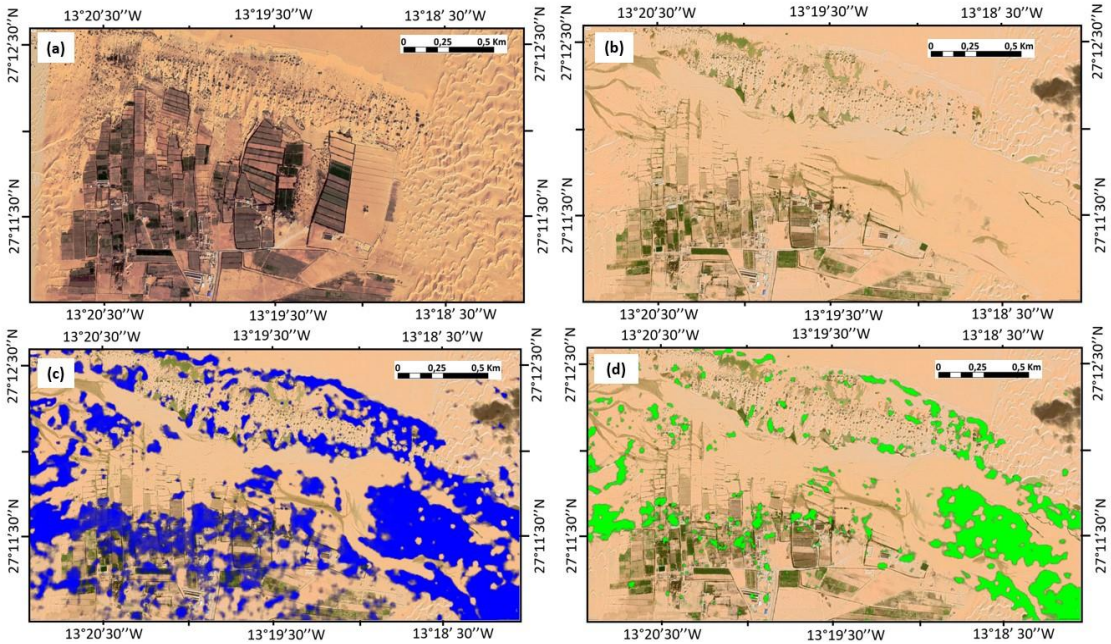


Fig. 8. Successively before (a) and after flood (b), NDFI (c) and NDFVI (d) showing flood damage near the city of Laayoune.

7. CONCLUSION

In this study, we applied a mapping methodology based on statistical analysis of time series for flood mapping in the Saharan environment. We used Sentinel-1 data and processed them with methods based on open-source software easily achievable also by the community of non-specialized experts in remote sensing of the flooded area in 2016, the city of Laayoune, southern Morocco (**Fig. 8**). The C band of Sentinel-1, operating at a wavelength of 5.7 cm, has a high sensitivity to surface water content as observed by radar. This band was used to measure soil moisture and flood detection. In the filtered and geocoded reference images, the smoothest surfaces appear very dark (Bragg scattering), attesting to the fact that the penetration depth of radar waves in this bare and dry soil can be quite deep. The rough surfaces appear very bright, corresponding to a corridor of moving sand dunes. These have different geometric and dielectric properties, with backscattering on rough surfaces. With the same textural properties on the soil, images taken after the rainy flood period show a strong backscattering of the radar signal. This confirms first that the dielectric properties of the soil depend on its water content, that the backscattering coefficient measured by radar instruments increases with increasing soil moisture and that the optimal threshold ranges for SAR data used in this analysis, can be the outline of a classification of flooded areas in desert context.

Two indices are proposed for flooded area mapping: the Normalized Difference Flood Index (NDFI) allowed the mapping of open water and the Normalized Difference Flood Index in Vegetation (NDFVI) for mapping shallow water in short vegetation and generating flood maps. These methods have made it possible to highlight the course of the watercourse, which is usually dry until flood periods as well as the stagnant water bodies in many closed depressions. The position of the

depressions show that they come from the dislocation of an organized hydrographic network, by capture, by exhaustion of the flow or by drying of the climate. This also gives an idea of the rate of accumulation of sand in the depressions and lowlands. The accumulations of sand would have been responsible for the concentration of groundwater in the substrate. This perfectly illustrates the interaction between wind and fluvial processes through the accumulation of sand resulting from a wind and fluvial process during dry conditions alternating with humid climatic episodes and the return of the fluvial system. This analysis can be generalized for the Saharan regions where wind activities and the return of the fluvial system interact during flood periods for the purpose of modeling, which is highly requested by the intervention organizations concerned, managers and scientists. In these regions, the correlation between the probability of groundwater in depressions and substantial sand accumulations appears to be a crucial consideration in the exploration of progressively scarce water resources.

REFERENCES

- Alsdorf DE., Rodríguez E., & Lettenmaier DP., (2007) Measuring Surface Water from Space. *Reviews of Geophysics*, 45, DOI:10.1029/2006RG000197.
- Álvarez-Mozos J., Casali J., González-Audícana M., & Verhoest N.E.C. (2005) Correlation between Ground Measured Soil Moisture and RADARSAT-1 Derived Backscattering Coefficient over an Agricultural Catchment of Navarre (North of Spain). *Biosystems Engineering*, 92, 119–133, DOI: 10.1016/j.biosystemseng.2005.06.008.
- Amimi T., Ouhnine R., Chao J., Elbelhiti H., & Koffi AS. (2017) Potentialités de l'écotourisme et géotourisme aux provinces de Tantan, Tarfaya et Layoune (Sahara Atlantique marocain). *European Scientific Journal*. Edition Vol.13, No.15 ISSN: 1857- 7881 (Print) e - ISSN 1857- 7431.
- Arnesen AS., Silva TSF., Hess LL., Novo EMLM., Rudorff CM., Chapman BD., & McDonald KC., (2013) Monitoring Flood Extent in the Lower Amazon River Floodplain Using ALOS/PALSAR ScanSAR Images. *Remote Sensing of Environment*. 130, 51–61, DOI: 10.1016/j.rse.2012.10.035.
- Borghys D., Yvinec Y., Perneel C., Pizurica A., & Philips W., (2006) Supervised Feature-Based Classification of Multi-Channel SAR Images. *Pattern Recognition Letters*. 27, 252–258, DOI: 10.1016/j.patrec.2005.08.006.
- Cian F., Marconcini M., Ceccato P., (2018) Normalized difference flood index for rapid flood mapping: Taking advantage of EO big data. *Remote Sens. Environ*. 209, 712–730.
- Dellepiane S., Bo G., Monni S., & Buck C., (2000) SAR Images and Interferometric Coherence for Flood Monitoring. In Proceedings of the IGARSS 2000. *IEEE 2000 International Geoscience and Remote Sensing Symposium*. Taking the Pulse of the Planet: The Role of Remote Sensing in Managing the Environment. Proceedings (Cat. No.00CH37120). Vol. 6, pp. 2608–2610 vol.6.
- Dellepiane SG., & Angiati E., (2012) A New Method for Cross-Normalization and Multitemporal Visualization of SAR Images for the Detection of Flooded Areas. *IEEE Transactions on Geoscience and Remote Sensing*. 50, 2765–2779, DOI:10.1109/TGRS.2011.2174999.
- Di Baldassarre G., Schumann G., Brandimarte L., & Bates P., (2011) Timely Low Resolution SAR Imagery To Support Floodplain Modelling: A Case Study Review. *Surv Geophys* 2011, 32, 255–269, DOI:10.1007/s10712-011-9111-9.
- Dong Y. B., Li M. J., Sun Y., (2013) Research on Threshold Segmentation Algorithms. *Advanced Materials Research*, DOI:10.4028/www.scientific.net/AMR.860-863.2888.
- ESA. (2022b). Mission ends for Copernicus Sentinel-1B satellite. [Online]. ESA. Last Updated: 3 August 2022. Available at: https://www.esa.int/Applications/Observing_the_Earth/Copernicus/Sentinel1/Mission_ends_for_Copernic [Accessed 12 August 2022].
- Franceschetti G., & Lanari R. (1999) *Synthetic Aperture Radar Processing*. Taylor & Francis Group, 324 pp, ISBN 9780203737484, <https://doi.org/10.1201/9780203737484>

- Hakdaoui S., Emran A., Pradhan B., Lee C.-W., & Nguemhe Fils, S.C., (2019) A Collaborative Change Detection Approach on Multi-Sensor Spatial Imagery for Desert Wetland Monitoring after a Flash Flood in Southern Morocco. *Remote Sens.* 2019, 11, 1042. <https://doi.org/10.3390/rs11091042>
- Henshaw, A.J.; Gurnell, A.M.; Bertoldi, W.; Drake, N.A. An Assessment of the Degree to Which Landsat TM Data Can Support the Assessment of Fluvial Dynamics, as Revealed by Changes in Vegetation Extent and Channel Position, along a Large River. *Geomorphology* **2013**, *202*, 74–85.
- Horritt M.S., (1999) A Statistical Active Contour Model for SAR Image Segmentation. *Image and Vision Computing* 1999, 17, 213–224, DOI:10.1016/S0262-8856(98)00101-2.
- Horritt M.S., Mason D.C., & Luckman A.J., (2001) Flood Boundary Delineation from Synthetic Aperture Radar Imagery Using a Statistical Active Contour Model. *International Journal of Remote Sensing* 2001, 22, 2489–2507, DOI:10.1080/01431160116902.
- Hostache R., Matgen P., & Wagner W., (2012) Change Detection Approaches for Flood Extent Mapping: How to Select the Most Adequate Reference Image from Online Archives? *International Journal of Applied Earth Observation and Geoinformation* 2012, 19, 205–213, DOI: 10.1016/j.jag.2012.05.003.
- IPR. (2022). Roughness and Brightness of SAR Image. [Online]. IPR: Quick Image Processing Research Guide. Last Updated: 5 February 2022. Available at: <https://www.gofastresearch.com/2022/02/roughness-and-brightness-of-sar-image.html> [Accessed 10 August 2022].
- Lasne Y., Paillou P., Freeman A., Farr T., McDonald K., Ruffié G., Malezieux J.M., & Chapman B., (2009) Study of hypersaline deposits and analysis of their signature in airborne and spaceborne SAR data: Example of Death Valley, California. *IEEE Trans. Geosci. Remote Sens.* 2009, 47, 2581–2598. [Google Scholar] [CrossRef]
- Liew S.C., (2001). SAR Images. [Online]. CRISP: Centre for Remote Imaging, Sensing and Processing. Available at: https://crisp.nus.edu.sg/~research/tutorial/sar_int.htm [Accessed 10 August 2022].
- Long S., Fatoyinbo T.E., & Policelli F., (2014) Flood Extent Mapping for Namibia Using Change Detection and Thresholding with SAR. *Environ. Res. Lett.* 2014, 9, 035002, DOI:10.1088/1748-9326/9/3/035002.
- Lu J., Giustarini L., Xiong B., Zhao L., Jiang Y., & Kuang G., (2014) Automated Flood Detection with Improved Robustness and Efficiency Using Multi-Temporal SAR Data. *Remote Sensing Letters* 2014, 5, 240–248, DOI:10.1080/2150704X.2014.898190.
- Manjusree, P., Prasanna Kumar, L., Bhatt, C.M., Rao G.S., & Bhanumurthy V., (2012) Optimization of threshold ranges for rapid flood inundation mapping by evaluating backscatter profiles of high incidence angle SAR images. *Int J Disaster Risk Sci* **3**, 113–122. <https://doi.org/10.1007/s13753-012-0011-5>.
- Martinez J.-M., & Le Toan T., (2007) Mapping of Flood Dynamics and Spatial Distribution of Vegetation in the Amazon Floodplain Using Multitemporal SAR Data. *Remote Sensing of Environment* 2007, 108, 209–223, DOI: 10.1016/j.rse.2006.11.012.
- Martinis S., Twele A., & Voigt S., (2011) Unsupervised Extraction of Flood-Induced Backscatter Changes in SAR Data Using Markov Image Modeling on Irregular Graphs. *IEEE Transactions on Geoscience and Remote Sensing* 2011, 49, 251–263, DOI:10.1109/TGRS.2010.2052816.
- Mason D.C., Horritt M.S., Dall’Amico J.T., Scott T.R., & Bates P.D., (2007) Improving River Flood Extent Delineation from Synthetic Aperture Radar Using Airborne Laser Altimetry. *IEEE Transactions on Geoscience and Remote Sensing* 2007, 45, 3932–3943, DOI:10.1109/TGRS.2007.901032.
- Mazel D., Fernez M., Meunier C., (2019) Protection contre les inondations du projet de la Technopole de Fom El Oued (Maroc), une évidence ?. Dignes Maritimes et Fluviales de Protection contre les Inondations, 2019 Version finale DOI : 10.5281/zenodo.2558162.
- Mertes L. A. K., (2002) Remote Sensing of Riverine Landscapes -” *Freshwater Biol.*, Vol. 47, No. 4, 2002, 799–816.
- Monographie de la région Laayoyne-Sakia-El Hamra. Direction Régionale de Laayoune. Haut-Commissariat au Plan. 2020. <https://www.hcp.ma/region-laayoune/attachment/2258177/>
- Nico G., Pappalepore M., Pasquariello G., Refice A., & Samarelli S., (2000) Comparison of SAR Amplitude vs. Coherence Flood Detection Methods - A GIS Application. *International Journal of Remote Sensing* 2000, 21, 1619–1631, DOI:10.1080/014311600209931.
- Pierdicca N., Pulvirenti L., Chini M., Guerriero L., & Candela L., (2013) Observing Floods from Space: Experience Gained from COSMO-SkyMed Observations. *Acta Astronautica* 2013, 84, 122–133, DOI: 10.1016/j.actaastro.2012.10.034.

- Pulvirenti L., Pierdicca N., Chini M., & Guerriero L., (2011) An Algorithm for Operational Flood Mapping from Synthetic Aperture Radar (SAR) Data Using Fuzzy Logic. *Natural Hazards and Earth System Sciences* 2011, 11, 529–540, DOI:10.5194/nhess-11-529-2011.
- Pulvirenti L., Pierdicca N., Chini M., & Guerriero L., (2013) Monitoring Flood Evolution in Vegetated Areas Using COSMO-SkyMed Data: The Tuscany 2009 Case Study. *IEEE Journal of Selected Topics in Applied Earth Observations and Remote Sensing* 2013, 6, 1807–1816, DOI:10.1109/JSTARS.2012.2219509.
- Ratschiller L.K., (1970) Lithostratigraphy of the Northern Sahara Spanisch. *Memoria Museo Tridentino Di Scienze Naturali Trento*, 1970, 18, 9–78.
- Rosenqvist A., Perez A., & Olfindo N., (2018). A Layman's Interpretation Guide to L-band and C-band Synthetic Aperture Radar data. *Committee on Earth Observation Satellites: Washington, DC, USA*.
- Schumann G., Bates P.D., Horritt M.S., Matgen P., & Pappenberger F., (2009) Progress in Integration of Remote Sensing-Derived Flood Extent and Stage Data and Hydraulic Models. *Reviews of Geophysics* 2009, 47, DOI:10.1029/2008RG000274.
- Schumann G.J.-P., & Moller D.K., (2016) Microwave Remote Sensing of Flood Inundation. *Physics and Chemistry of the Earth, Parts A/B/C* 2015, 83–84, 84–95, DOI: 10.1016/j.pce.2015.05.002.
- Smith L.C., (1997) Satellite Remote Sensing of River Inundation Area, Stage, and Discharge: A Review. *Hydrol. Process.*, 11 (10) (1997), 1427-1439, 10.1002/(Sici)1099-1085(199708)11:10<1427: Aid-Hyp473>3.0. Co;2-s 1997.
- Tiepolo M., (2014) Flood Risk Reduction and Climate Change in Large Cities South of the Sahara. In *Climate Change Vulnerability in Southern African Cities: Building Knowledge for Adaptation*; Macchi, S., Tiepolo, M., Eds, Springer Climate; *Springer International Publishing: Cham*, 2014; pp. 19–36 ISBN 978-3-319-00672-7.
- White I., (2013) *Water and the City: Risk, Resilience and Planning for a Sustainable Future*; Routledge, 2013; ISBN 978-1-136-94749-0.
- Xue F., Gao W., Yin C., Chen X., Xia Z., Lv Y., Zhou Y., & Wang M., (2022) Flood Monitoring by Integrating Normalized Difference Flood Index and Probability Distribution of Water Bodies. *IEEE Journal of Selected Topics in Applied Earth Observations and Remote Sensing* 2022, 15, 4170–4179, DOI:10.1109/JSTARS.2022.3176388.